Strong constraints on primordial black hole dark matter from 16 years of INTEGRAL/SPI observations

J. Berteaud,[1,*] F. Calore,[1,†] J. Iguaz,[1,‡] P. D. Serpico,[1,§] and T. Siegert[2,3,‖]

[1]*LAPTh, CNRS, USMB, F-74940 Annecy, France*
[2]*Institut für Theoretische Physik und Astrophysik, Universität Würzburg, Campus Hubland Nord, Emil-Fischer-Strasse 31, 97074 Würzburg, Germany*
[3]*Max Planck Institut für extraterrestrische Physik, Gießenbachstrasse 1, 85748 Garching bei München, Germany*

(Received 24 February 2022; accepted 11 July 2022; published 27 July 2022)

We present a new analysis of the diffuse soft γ-ray emission toward the inner Galaxy as measured by the spectrometer aboard the INTEGRAL satellite (SPI) with 16 years of data taking. The analysis implements a spatial template fit of SPI data and an improved instrumental background model. We characterize the contribution of primordial black holes (PBH) as dark matter (DM) candidates evaporating into $\mathcal{O}(1)$ MeV photons by including, for the first time to our knowledge, the spatial distribution of their signal into the fitting procedure. No PBH signal is detected, and we set the strongest limit on PBH DM for masses up to 4×10^{17} g, significantly closing in to the so-called asteroid mass range.

DOI: 10.1103/PhysRevD.106.023030

I. INTRODUCTION

A long-standing, paradigmatic nonparticle candidate for the dark matter (DM) in the universe is constituted by primordial black holes (PBHs) (see Ref. [1] for a recent review). Such objects could have arisen in the early universe from the gravitational collapse of overdensities made of *ordinary* radiation and/or matter, associated, for instance, with large density fluctuations at small scales set by nonminimal inflationary settings or with phase transitions. While most of the PBH DM parameter space is excluded or tightly constrained by a number of observations, a window of masses between about 10^{17} g and 10^{23} g, i.e., the *asteroid* mass range, is still potentially viable. The upper range of this window can be tested via high-cadence microlensing surveys, and the lower part is accessible via high-energy astrophysical probes, sensitive to their Hawking evaporation spectrum, falling in the hard x-ray to the soft γ-ray band. Large fields of views and high statistics measurements in this observationally challenging window are required to tighten this probe. One instrument with appropriate characteristics is the coded-mask spectrometer telescope, SPI, aboard the INTEGRAL satellite [2,3]. SPI surveys the γ-ray sky with a focus on the Galactic bulge and disk and, with a forward application of the imaging response, can observe diffuse emission such as expected from cosmic-ray interactions with gas and radiation fields or from the distribution of DM in the Milky Way.

We present here the first, dedicated, SPI analysis of PBH DM in the Milky Way: The spatial distribution of the PBH mega-electron-volt (MeV) signal is considered as an independent *template* in the fit of SPI data, as it is done for other known astrophysical components, such as the diffuse inverse Compton (IC) scattering along the Galactic plane, or the positronium (Ps) emission with a strong γ-ray line at 511 keV. We go beyond previous approaches, in particular Ref. [4], where the limits on PBH DM are inferred from a measurement of the soft γ-ray diffuse emission derived with SPI data using a set of templates that do not account for a PBH component. Consequently, the limits derived with such an approach may be biased, since the additional PBH contribution is neglected in the set of templates adopted. Note that the PBH evaporation emission has a specific *morphology*, following generic DM density profiles, e.g., a Navarro-Frenk-White (NFW) profile [5], which must be taken into account to derive a fully self-consistent limit on the PBH parameter space. SPI analyses are challenging and require great carefulness: Besides diffuse astrophysical fluxes, several hundreds of (variable) point sources contribute to the total signal, especially at energies $\lesssim$300 keV. This is particulary relevant for constraining higher PBH masses, since the PBH blackbody temperature decreases with mass as $T_{\rm PBH} \propto M_{\rm PBH}^{-1}$.

This article is structured as follows: Sec. II describes our new SPI template analysis. Section III is a compact

*berteaud@lapth.cnrs.fr
†calore@lapth.cnrs.fr
‡iguaz@lapth.cnrs.fr
§serpico@lapth.cnrs.fr
‖tho.siegert@gmail.com

description of the spectral components entering the fit to the total spectrum. Section IV presents our results, while Sec. V includes a discussion and conclusions. Further technical information is provided in the appendixes: Appendix A describes the dataset and its handling, Appendix B is devoted to the template fitting procedure and systematic uncertainties, while Appendix C includes further details on the spectral fitting procedure and results, including astrophysical background components.

II. NEW SPI TEMPLATE ANALYSIS OF DIFFUSE γ RAYS

We analyzed 16 years of data taken by SPI over the energy range 30 keV–8 MeV, extending to low energies the new measurement of the diffuse soft γ-ray emission with SPI between 0.5 and 8 MeV recently performed by some of the authors in Ref. [6]. The lower energy limit is such to avoid source confusion especially toward the Galactic Center and to guarantee correct energy calibration and detector performance.

Our analysis relies on an improved description of the instrumental background (BG) [7,8] and a systematic study of the dominating diffuse IC scattering emission that originates from cosmic-ray electrons in the GeV range produced by standard astrophysical sources in the Galactic disk. Details on the dataset used can be found in Appendix A.

Our SPI data analysis relies on the comparison of models, i.e., images, and a description of the instrumental BG, to data in a raw format, here the number of photons detected per unit observation per detector per energy bin. The images (spatial templates or morphologies) are convolved through the SPI coded-mask response, which depends on the source aspect angle and the photon energy. The BG model contains all the knowledge about the instrument, the detectors, and their behavior over the full SPI data taking period. The models can then be considered as time series of expected detector patterns that are fitted to the measured time series via a maximum likelihood approach, using the Poissonian likelihood. This is done energy bin by energy bin independently to extract the spectrum of the template maps included and to obtain the total flux. So, unlike in the case of the *Fermi* Large Area Telescope (LAT), where the measured counts are projected onto a sky map and where the resulting image is interpreted in terms of different templates, SPI can hardly provide morphology-independent spectra nor spectrum-independent morphologies with the current standard software, OSA/*spimodfit*[1] [9,10]. Instead, the spatial templates for one or more components are assumed and fitted to the raw data to obtain their flux contribution. Spectral fits on the components that have been separated via angular templates are performed in a second step, described in Sec. III.

Considering the fully coded SPI field of view of $16° \times 16°$ and the partially coded (i.e., without all detectors exposed to the source) field of view of $30° \times 30°$, we select a *region of interest* (ROI) in this analysis of $|l| \leq 47.5°$, $|b| \leq 47.5°$. This is the range over which we calculate our spatial templates.

Besides the instrumental BG, SPI data are fitted with a model for astrophysical sources of MeV photons. Below ~ 300 keV, the total emission is dominated by point sources [11]. We assume that all sources included in this study are constant in time. This means an average of the sources' fluxes is extracted. This can partially impact the diffuse emission components in particular below $\sim$50 keV. We adopt an iterative approach (similar to [10]) to determine the contribution of point sources at each energy. This means we use the compiled SPI source catalog from Ref. [11], including 256 known sources for the full sky, and fit the total model, i.e., all diffuse components (see next paragraph) plus point sources plus instrumental BG, per energy bin. Unless a source is detected with more than 2σ in two subsequent energy bins, we drop the source to reduce the number of fitted parameters for the next-higher energy bin. The point source positions are taken from [11] so that the resulting diffuse spectrum is, indeed, similar to the one in [11]. Besides, because of the source variability, our method includes a certain higher degree of systematics compared to [12], but because we know where the sources are statistical uncertainties are reduced. We find sources up to $\sim$1 MeV in our ROI. However, because of source confusion and the limits of our method to handle more than 10000 parameters, we get a reliable estimate of point source fluxes only above 50 keV.

To extract the total diffuse spectrum we consider the following spatial components: (1) A population of unresolved point sources (mostly cataclysmic variables, CVs) up to $\sim$100 keV [13]; (2) the Ps emission including continuum up to 511 keV and the 511 keV line [14]; (3) the ^{26}Al line at 1809 keV from massive stars [15]; (4) the diffuse IC scattering continuum in the whole spectral range [6]; (5) the expected morphology from evaporating PBHs, tracking the conventional NFW halo for DM distribution, detailed in the following; see also Fig. 4 in Appendix B. For the most prominent IC emission, we consider four different models and use, as input for the SPI analysis, soft γ-ray maps obtained from the GALPROP v56 cosmic-ray propagation code (see [16]). These very same models have been used for the dedicated high-energy SPI analysis of Ref. [6]. The basic details of the adopted IC models are summarized in Appendix B, and we also provide the corresponding *galdef* input files in a public Zenodo repository. We stress that the choice of these four models, while not representing an exhaustive scan over the systematic uncertainties induced by cosmic-ray

[1]User manual available at http://isdc.unige.ch/integral/download/osa/doc/11.0/spimodfit_handbook.pdf.

propagation, is nonetheless sufficient to assess the impact of variations of the IC morphology on the PBH signal evidence and bounds. As shown in Ref. [6], these models do indeed predict different IC morphologies (with variations also reaching up 50%–60%) which induce a systematic uncertainty of 30% at most on the extracted MeV fluxes in the range where IC is dominant. We anticipate that the propagated effect of IC systematic uncertainty on PBH bounds is at the tens of percent level, and so, while important for the *interpretation* of any mismatch between GALPROP-based predictions and data, a more systematic scan of the cosmic-ray production and propagation parameter space is beyond the scope of this paper.

Being interested in PBH as possible DM candidates, we assume that their spatial number density in the Galaxy follows a typical NFW DM profile [5]. We use the following parameter values: $r_s = 9.98$ kpc for the scale radius, and $\rho_s = 2.2 \times 10^{-24}$ g/cm^3, in agreement with a recent fit to Milky Way dynamical data [17].

The diffuse γ-ray flux from Galactic PBH evaporation writes as

$$\frac{\mathrm{d}\Phi_\gamma}{\mathrm{d}E}(l,b) = \frac{f_{\mathrm{PBH}}}{4\pi M_{\mathrm{PBH}}} \frac{\mathrm{d}^2 N_\gamma}{\mathrm{d}E\mathrm{d}t} \int_{\mathrm{l.o.s.}} \mathrm{d}s \rho(r(s,l,b)). \quad (1)$$

It receives contributions from (a) a *normalization* factor depending on the PBH mass and fraction of PBHs that may be the DM in the universe (f_{PBH})—the parameter we want ultimately to constrain; (b) a M_{PBH}-dependent *spectral* term, which defines the energy dependence of the signal, discussed below; and (c) a *spatial* term, which corresponds to the integral along the line of sight (l.o.s.) of the DM profile—also known in the DM literature as the $\mathcal{D}$ factor, which determines the morphology of the signal. Note that, because of the detection technique, the analysis is insensitive to isotropic contributions, such as the extragalactic contribution or the isotropic residual of the Galactic halo, which are thus eliminated from our NFW model template.

For the sake of our analysis, we notice that the spectral and spatial terms in Eq. (1) factorize, so that only the l.o.s. dependent $\mathcal{D}$ factor enters in the definition of the PBH template used as input for the SPI analysis (see below). The spectral term, instead, will be fully exploited only when setting constraints on the PBH parameter space.

We perform the integral along any given direction in the analysis ROI to get a map of the expected spatial distribution of the PBH signal. The map is binned in $0.5° \times 0.5°$pixels and centered on the Galactic Center for both b and l, thus including $\mathcal{O}(40000)$ pixels.

III. SPECTRAL FITS OF THE TOTAL SPECTRUM

Once the components have been separated via angular templates, Sec. II, a spectral fit to the total spectrum is performed to derive the parameters of interest for the spectral model. In the spectral analysis, the astrophysical components are fitted with the following: (1) The population of unresolved point sources, believed to be mostly CVs and stars with hot coronae [18], is parametrized via a cutoff power law with free normalization and cutoff energy; (2) positron annihilation, allowing for a free normalization of the 511 keV line and a free fraction of ortho-Ps controlling the continuum emission below 511 keV; (3) nuclear lines, with a free normalization; and (4) IC with a power law, with free amplitude and index. We refer the interested reader to Appendix C for more technical details of the spectral fit.

The PBH emission is predicted to come from *Hawking radiation* [19], with a spectrum following an almost blackbody distribution, with temperature given in natural units by $T_{\mathrm{PBH}} = M_P^2/(8\pi M_{\mathrm{PBH}})$, where M_P is the Planck mass:

$$\frac{\mathrm{d}^2 N_i}{\mathrm{d}E\mathrm{d}t} = \frac{1}{2\pi} \frac{\Gamma_i(E, M_{\mathrm{PBH}})}{e^{E/T_{\mathrm{PBH}}} - (-1)^{2s}}. \quad (2)$$

In the spectrum given by Eq. (2), s is the spin of the ith radiated particle, E is its energy, and $\Gamma_i(E, M_{\mathrm{PBH}})$ is a species-dependent graybody factor. To compute the spectrum of photons from Hawking evaporation of PBHs, we use BLACKHAWK v1.2 [20]. We only consider the primary spectrum since the extrapolation tables used to compute secondary photons lead to unphysical spectra in the relevant range of energies. We note that the authors of Ref. [20] released an upgraded version (`v2.1`) of the software which includes a new tool to compute the secondary photon spectra more reliably. However, this contribution only has an effect on the low energy tail of spectra for the lowest PBH masses considered here. Therefore, our results are not significantly altered by such an update of the code, as also shown in [21].

Spectral parameters are sampled following the EMCEE Markov chain Monte Carlo sampling method [22] within the *3ML* package [23] and allowed to vary within a broad prior range, only preventing unphysical, e.g., negative, fluxes.

IV. RESULTS

We first report our results about the angular decomposition and template analysis to extract the flux components; cf. II. We first consider template components (1)–(4) in Sec. II and perform the spectral extraction of the components. The IC emission is the dominant contribution to the soft γ-ray diffuse emission. All IC models perform equally well in describing SPI data; however, the extracted spectra show variations on the order of 5%–20% above 0.5 MeV, and about 30%–50% below 0.5 MeV. We use these variations among IC models to assess the systematic uncertainties affecting the spectral extraction. The total flux is hardly dependent on the chosen IC morphology, except for the range around 100–250 keV because the maximum

number of templates contributes there. We also note that in the lowest two energy bins, 30–50 keV, the degeneracy among the fitted components is large compared to the remaining part of the spectrum, resulting in 2 orders of magnitude higher systematics. Hence, we conservatively omit this band from our spectral fits. We show the extracted flux for the total spectrum in Fig. 2 (left panel), including systematic uncertainties that come from the variation of IC. As a second step, in addition to the already known components of the Galactic flux as discussed above, we include the l.o.s.-integrated NFW profile as a template for PBH DM in the SPI analysis, and we extract the corresponding total spectrum of the diffuse soft γ-ray emission. Fitting an NFW profile at each energy bin leads to *no detection*—regardless of what IC model we adopt. We can therefore set 95% C.L. upper limits on the γ-ray flux from DM PBH, which is shown in Fig. 2 (right panel). The upper limits on the flux originating from a NFW template are robust (typically within 5%–20%, depending on the energy, hence PBH mass) with respect to the chosen IC spectral model.

We now discuss spectral fits; cf. Sec. III. Let us focus first on the total spectrum extracted including the astrophysical spectral components (1)–(4); cf. Sec. III. The fitted spectrum compares well to previous analyses, e.g., Refs. [10,11,24]. We notice an overall good agreement, with departures from the fit within the 2σ level, keeping in mind that some contribution expected from positron annihilation in flight (see, e.g., [25–27]) is neglected in this analysis. We have a satisfactory fit over the full energy range, although low-energy and high-energy data seem to prefer different IC models as best fit, which may indicate a (statistically not significant) departure from a single power-law parametrization of the IC spectrum in this range. For a more thorough comparison in the high-energy range, we refer the reader to Ref. [6], while we discuss the low-energy range in Appendix B.

Analogous to what has been done before, we fit the total spectrum obtained including *all* template components with the generic model presented earlier together with the expected PBH spectrum, Eq. (1); see Fig. 1. As for PBH, the free spectral parameters are the PBH DM abundance, $f_{\rm PBH}$, sampled from a log-uniform distribution, and the logarithm of the PBH mass, sampled from a uniform distribution.[2] Given the null evidence for the PBH component, we achieve a comparably satisfactory fit when including PBH with respect to the model with astrophysical components only. This spectral fit also allows us to derive constraints on the PBH DM abundance: For each mass value, the constraints on the PBH DM abundance are defined such as they separate 95% of the samples with the lowest $f_{\rm PBH}$ values from the 5% with the highest ones. In Fig. 1, we display the fit to the total spectrum for the highest excluded PBH mass, $M_{\rm PBH} \simeq 4 \times 10^{17}$ g.

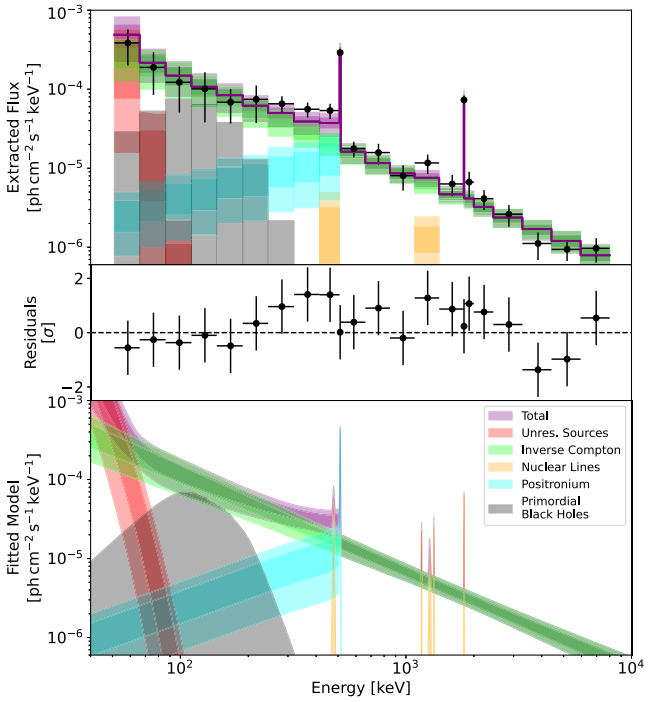

FIG. 1. Extracted spectral data points and fit to the total diffuse emission spectrum (top) with residuals (center) and fitted model components (bottom). Shown are the 1 and 2σ bands for the detected components. We also display the 2σ upper limit from our highest excluded PBH mass at $\sim 4 \times 10^{17}$ g. See legend and main text for details. The tabulated spectra of the different components can be found in the public Zenodo repository.

In Fig. 3, we show our main result: We exclude that PBHs account for all the DM in the universe up to masses of $\simeq 4 \times 10^{17}$ g. Compared to existing bounds, a selection of which is also reported in Fig. 3,[3] ours exclude the largest PBH masses in the low-mass window to date, and significantly closes in to the right into the asteroid mass range. Note that the comparatively weaker bounds between 2×10^{16} g and 10^{17} g are due to the fact that for most masses in this range a PBH contribution would partially fill in the small excesses in the residuals between 300 keV and a few MeV visible in Fig. 1.

V. DISCUSSION AND CONCLUSIONS

The results obtained are robust against a number of systematic checks we performed. For instance, removing

[2]Please note that this two-parametric bound is not what is done typically in the literature, i.e., a one-parametric bound on $f_{\rm PBH}$ at a fixed mass. Our approach may lead therefore to slightly more conservative bounds.

[3]Further bounds relevant in this mass range are in [28–30]; other bounds from medium *heating* only extend to lower masses, but can go deeper in $f_{\rm PBH}$ space; see [31,32].

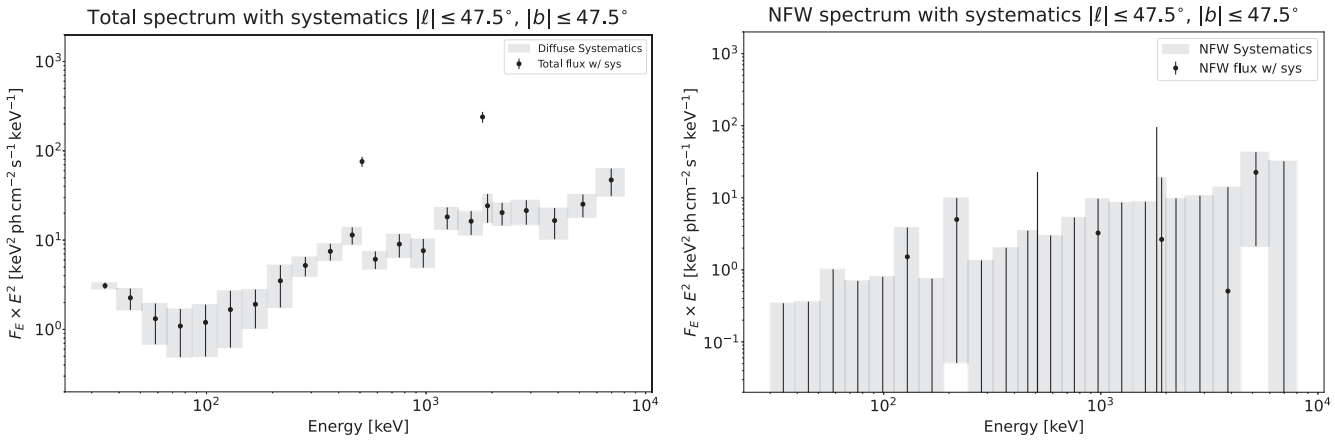

FIG. 2. Total (left) and NFW (right) extracted spectra including systematic uncertainties. Similar plots for the other template fit components are provided in Fig. 6 in Appendix B.

the first two energy bins (which are affected by the largest systematic uncertainties) from the total spectrum does not affect the limits. The limits are also robust against the choice of the prior on the PBH mass down to 1.8×10^{16} g. Furthermore, the limits are not very sensitive to the specific model of IC, among the ones we tested. We stress, however, that even in the case in which we neglect any astrophysical background spectral information in the limit-setting procedure and use the extracted NFW flux presented in Fig. 2, the limit would still exclude $f_{\rm PBH} = 1$ at $M_{\rm PBH} = 2 \times 10^{17}$ g; i.e., it would still remain the strongest limit on PBH constituting the totality of DM.

As common to all Galactic limits in the literature, translating the bounds on flux into bounds on $f_{\rm PBH}$ carries on the standard uncertainty related to the local DM density, of about 30%. Since we are focusing on a very large ROI (as opposed to the innermost Galaxy), the uncertainty due to the mere shape of the DM halo is mild: By considering a cuspier halo model (respectively, cored model) according to Table 1 of Ref. [36], we would infer 16% tighter (respectively, 10% looser) bounds.

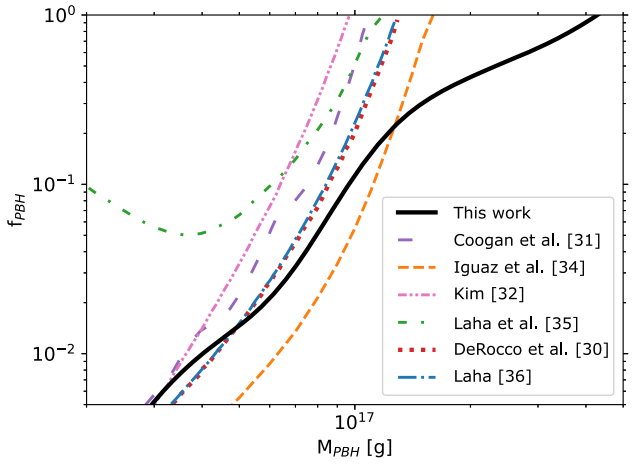

FIG. 3. The 95% C.L. upper limits on the fraction $f_{\rm PBH}$ of DM that can be composed of PBHs as a function of the PBH mass, $M_{\rm PBH}$, derived in this work (black solid line). We also show, from top to bottom, bounds from the literature derived in [30] (purple line), [33] from the cosmic x-ray background (orange line), [31] (pink line), [34] from diffuse soft γ rays using published SPI results (green line), [29] (red line), and [35] from 511 keV constraint (NFW "3 kpc" case, blu line).

We have not considered here photons that come from positrons, produced by PBH evaporation, annihilating with electrons of the interstellar medium in flight or at rest, and generating an additional diffuse continuum contribution or 511 keV line signal, respectively, as was performed in Ref. [27] for the case of the dwarf galaxy Reticulum II. Also, we neglect diffuse photons that come from positrons and electrons from PBHs which induce IC emission when scattered off by low ambient photons of the interstellar radiation field. We, indeed, explicitly checked that this contribution does not contain any additional constraining power for the SPI analysis: The MeV spectrum is sensitive only to the overall number of electrons and positrons injected and the level of reacceleration in the propagation model, and it is therefore highly uncertain as a probe of PBHs.

Also, we presented bounds for a monochromatic mass function. Relaxing this condition is expected to lead to mildly more stringent bounds. For instance, we checked that a log-normal mass distribution centered at $M_{\rm PBH} = 10^{17}$ g with a dimensionless width $\sigma \simeq 0.1$ would lead to $\sim$10% tighter bounds, which improve to a factor of $\sim$2 stronger bounds when $\sigma \gtrsim 0.3$. More stringent bounds are also obtained if going from nonrotating (Schwarzschild) PBH to rotating (Kerr) PBH; see, e.g., [33].

Let us briefly comment on some directions for improvements: On the one hand, the new SPI data points can be put into context of *Fermi*-LAT, COMPTEL [37], and eROSITA [38] diffuse emission measurements to evaluate how the IC modeling can be improved, and, ultimately, what are the consequences for PBH DM. In particular, if the diffuse

emission in the kilo-electron-volt band can be separated from the point sources, eROSITA might probe PBHs with masses around $\sim 10^{18}$ g, beyond current reach. On the other hand, if additional components, such as positron annihilation at rest or in flight from PBH are included, the limits are expected to be stronger. Nonetheless, computing the expected 511 keV signal is challenging given the highly uncertain propagation conditions in the interstellar medium at those energies.

Finally, we highlight that the new SPI template analysis developed here, which includes a template component for NFW DM, can be straightforwardly extended to set constraints on other generic models for decaying particle DM, and it is thus of broad interest. This strategy can also prove useful in pushing the sensitivity expected by future missions, as studied, e.g., in [30,39,40].

ACKNOWLEDGMENTS

F. C., J. B., and P. D. S. acknowledge support by the "Agence Nationale de la Recherche," Grant No. ANR-19-CE31-0005-01 (PI: F. Calore). T. S. acknowledges support by the Bundesministerium für Wirtschaft und Energie via the Deutsches Zentrum für Luft- und Raumfahrt (DLR) under Contract No. 50 OX 2201. This work made use of the GALPROP code for cosmic-ray propagation, [41].

APPENDIX A: INTEGRAL/SPI DATASET

The SPI dataset used here is identical to the one from Ref. [6] with an extension to lower energies, thus in total from 30 keV to 8 MeV. For completeness, we summarize the main characteristics in the following: We define 22 logarithmic energy bins and include two narrow bins to account for the 511 keV line from positron annihilation and the 1809 keV line from ^{26}Al decay. The two ^{60}Fe lines at 1173 and 1332 keV only show a significance of $\sim 5\sigma$ above the IC continuum when analyzed in combination [42]. We therefore omit cutting the intermediate energy bin from 1093 to 1404 keV into five individual bins as this would unnecessarily increase the uncertainties. Instead, we treat the ^{60}Fe lines in relation to the ^{26}Al line (see Appendix C) because they are expected to contribute to the flux in this energy bin. Other nuclear lines that might contribute to the diffuse emission such as from ^{7}Be at 478 keV and ^{22}Na at 1275 keV are also absorbed in the broad logarithmic energy bins, and treated individually in the spectral fit because their contributions were found to be negligible [43].

The total number of targeted observations in this dataset is 35892 pointings for the range above 514 keV and 34428 pointings for the range below. The dataset includes a dead-time corrected total exposure time of 65.3–68.5 Ms, depending on the energy range chosen, within a spherical rectangle of $\Delta l \times \Delta b = 95° \times 95°$ centered at the Galactic Center. To account for failures of the germanium detector, we separated the dataset in five different epochs, one for each camera configuration. The relative normalizations of the five different imaging responses are fixed by the official instrument response function distribution from the INTEGRAL Science Data Center.

TABLE I. Dataset characteristics. The columns from left to right are the energy band in units of keV, the number of data points, the background variability timescale in units of days, the corresponding number of dof, the calculated reduced χ^2 value from the best fit, the number of used point sources, and the SPI processing chain. The values from 514 to 8000 keV are the same as in Ref. [6] and only repeated here for consistency.

Energy band	n_{data}	T_{BG}	dof	χ^2/dof	n_{PS}	Proc.
39–51	556184	0.09	530703	⋯	109	SE
51–66	556184	0.19	542774	1.1328	92	SE
66–86	556184	0.19	542810	1.1622	56	SE
86–112	556184	0.19	542816	1.0889	50	SE
112–145	556184	0.75	551309	1.0137	44	SE
145–189	556184	0.75	551321	1.0139	32	SE
189–245	556184	1.5	553502	1.0135	21	SE
245–319	556184	0.75	551342	1.0038	11	SE
319–414	556184	1.5	553515	1.0029	8	SE
414–508	556184	1.5	553518	1.0062	5	SE
508–514	556184	3	554707	0.9912	4	SE
514–661	578764	0.75	573827	1.0059	4	PSD
661–850	578764	0.75	573827	0.9984	4	PSD
850–1093	578764	0.75	573831	0.9974	⋯	PSD
1093–1404	578764	0.75	573831	0.9974	⋯	PSD
1404–1805	578764	1.5	576047	0.9939	⋯	PSD
1805–1813	578764	3	577254	0.9935	⋯	PSD
1813–2000	578764	3	577255	0.9953	⋯	PSD
2000–2440	582349	6	581390	1.0057	⋯	HE
2440–3283	582349	3	580836	1.0040	⋯	HE
3283–4418	582349	3	580836	1.0026	⋯	HE
4418–5945	582349	3	580836	1.0064	⋯	HE
5945–8000	582349	6	581390	1.0038	⋯	HE

The background variability timescale from the background handling method in Ref. [8] changes quickly toward a higher variability the smaller the energy. We provide an overview of the number of fitted parameters, included components, degrees of freedom, background variability, and fit quality in Table I. Except for the energy bin 39–51 keV with the highest background variability and largest number of point sources, all energy bins show an adequate fit quality as measured by the reduced χ^2. Extracting the flux values and their uncertainties as a function of energy occurs in the native SPI data space, i.e., number of photons recorded per detector, energy, and pointing. Spectral fits (see Appendix C) are then performed in the reconstructed spectral domain.

APPENDIX B: EXTRACTED SPECTRA AND SYSTEMATIC UNCERTAINTIES

In Fig. 4 we show the diffuse emission models, i.e., templates, used in this work, and used for the spectral extraction, Sec. II.

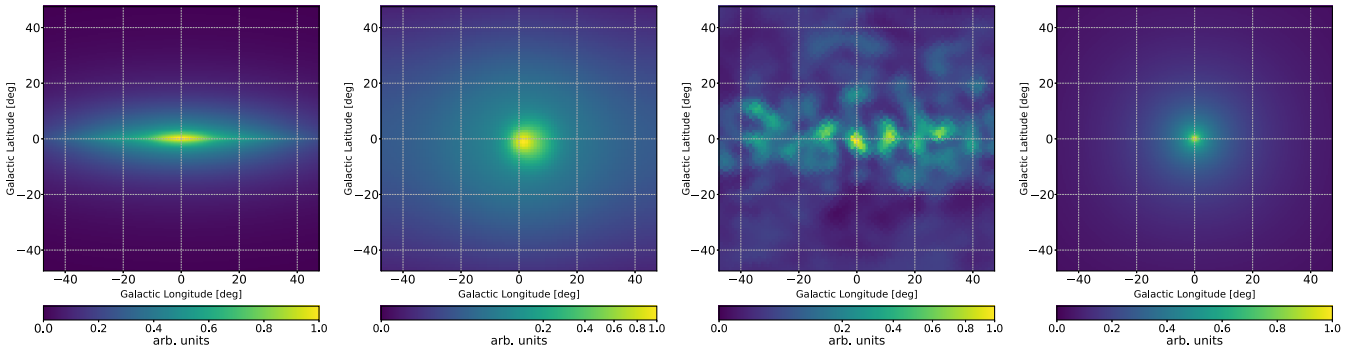

FIG. 4. Sky models used for the analysis. Shown are, from left to right, the IC emission model at 281 keV from the model variant $\delta_1 = \delta_2 = 0.5$ (see Ref. [6]), the positronium emission model from Ref. [14], the 1.8 MeV ^{26}Al map reconstructed from SPI data by Ref. [44], as well as a line-of-sight integrated NFW profile (see main text).

The systematic study of which diffuse emission model for the IC scattering component in the Milky Way best describes the lower energies of the SPI spectrum (30–514 keV) is detailed below. It follows the same thread as in a recent work about SPI's high-energy range (514–8000 keV) from Ref. [6]. We briefly summarize here the main features of the IC models we used. We consider the model ${}^{\mathrm{S}}\mathrm{S}^{\mathrm{Z}}4^{\mathrm{R}}20^{\mathrm{T}}150^{\mathrm{C}}5$ as defined in [45] which provides a good fit to *Fermi*-LAT γ-ray data. Based on the *Fermi* galdef file, we then create a model matching the parameters in Table 2 of [46], which is tuned to match low-energy cosmic-ray data from Voyager 1 (`voyager` baseline). To assess the systematic uncertainties from IC, we also define two additional models obtained varying some parameters of the `voyager` baseline: (i) $\delta_1 = \delta_2 = 0.5$, case of a single diffusion index as suggested by [47,48]; (ii) `ISRF` $\times$ 10, case with a factor of 10 stronger optical ISFR. All four models inherit the same cosmic-ray source distribution from ${}^{\mathrm{S}}\mathrm{S}^{\mathrm{Z}}4^{\mathrm{R}}20^{\mathrm{T}}150^{\mathrm{C}}5$, i.e., the SNR distribution from [49]. We made the GALPROP input, i.e., galdef, files of the models considered publicly available at Zenodo.

Another source of variations of the IC morphology can be, e.g., a different distribution of cosmic-ray sources. We explicitly checked that the variations induced on the IC morphology by assuming distributions L, Y, and O from [50] are at the level of 15%–20% at most with respect to our `voyager` baseline model. Therefore, they cannot dominate the systematic uncertainty of the extracted PBH flux, and, in turn, significantly alter the PBH bounds. Additionally, other untested effects are inhomogeneous diffusion and other propagation scenarios, e.g., addressed in [51–54]. We stress that, because of the poor SPI angular resolution and contrary to what occurs at GeV energies, different models at MeV energies carry larger degeneracies which are difficult to break; see Ref. [6] for a thorough discussion.

Within the systematic uncertainties, our IC model selection (`voyager` baseline, $\delta_1 = \delta_2 = 0.5$, `ISRF` $\times$ 10, ${}^{\mathrm{S}}\mathrm{S}^{\mathrm{Z}}4^{\mathrm{R}}20^{\mathrm{T}}150^{\mathrm{C}}5$) is consistent with previous studies, e.g., Ref. [11] within ∼25%. There is no single best IC model for the entire energy range of 30–8000 keV. At higher energies ($>$ 500 keV) model variant $\delta_1 = \delta_2 = 0.5$ fits best, whereas at lower energies `voyager` baseline and ${}^{\mathrm{S}}\mathrm{S}^{\mathrm{Z}}4^{\mathrm{R}}20^{\mathrm{T}}150^{\mathrm{C}}5$ are closest to the extracted flux data points from SPI. Because IC shows a known variation with energy and is, in addition, not well determined in the MeV range, we show, as an example, the differences in three of our models for 30 and 8000 keV, respectively, in Fig. 5.

In Fig. 6, the extracted spectra with systematics are shown for the individual components not presented in Fig. 2. As for the NFW template, there is no detection that could resemble the expected shape of PBH evaporation. A few energy bins (112–145 keV, 189–245 keV, and 4418–5945 keV) show more than 3σ deviations from zero. However, including the different IC model variants for the

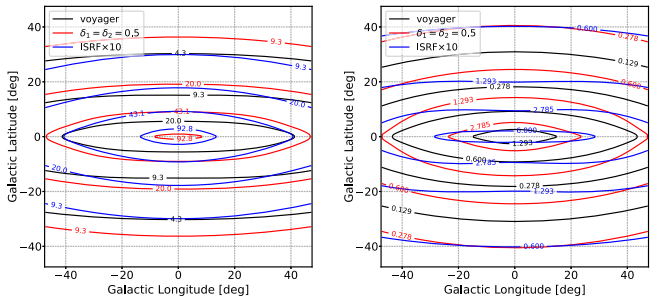

FIG. 5. Comparison of three different IC model configurations for 30 keV (left) and 8000 keV (right). The units of the contours are 10^{-4} ph cm^{-2} s^{-1} sr^{-1} and 10^{-7} ph cm^{-2} s^{-1} sr^{-1} for the 30 and 8000 keV figures, respectively.

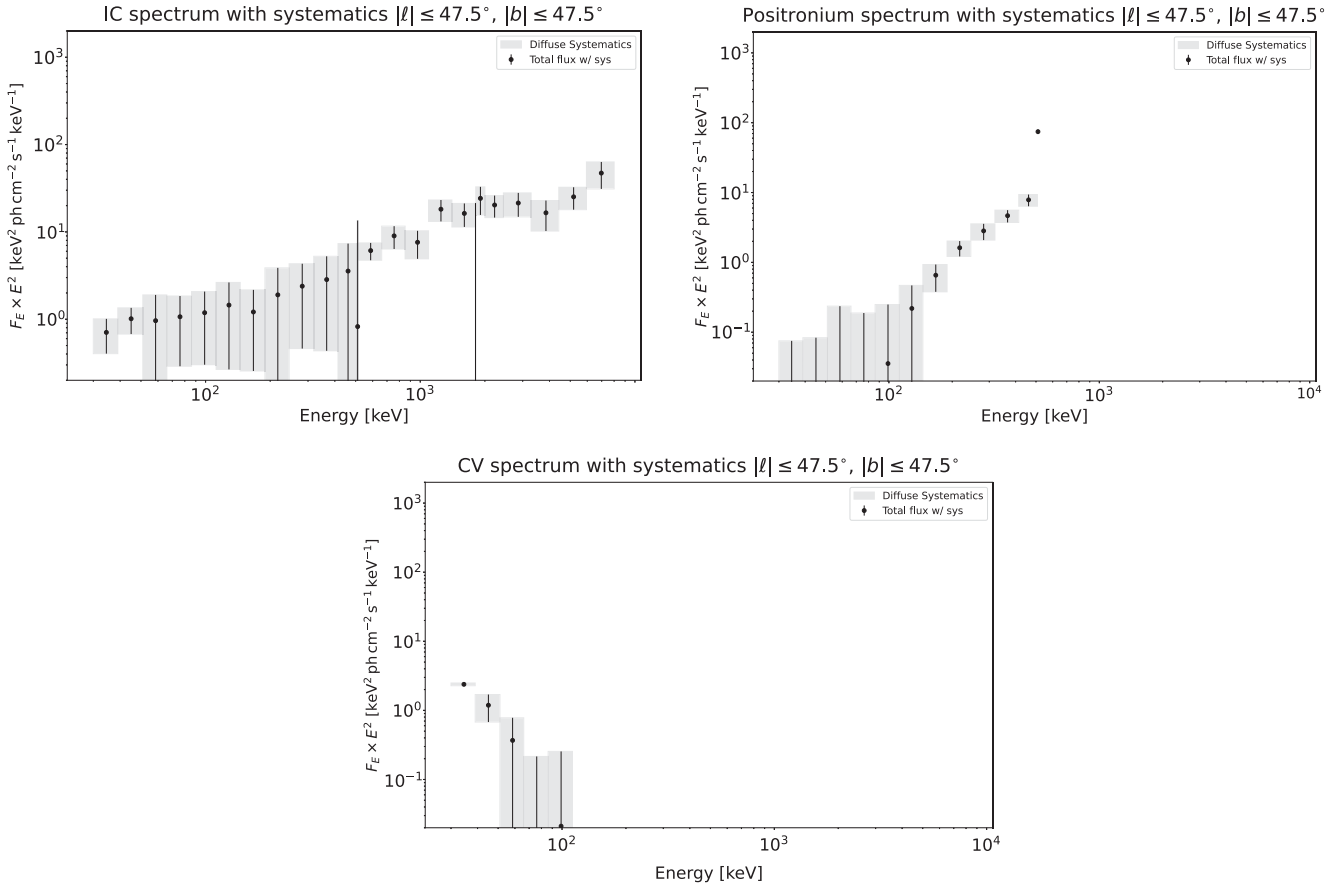

FIG. 6. Final spectra including systematics: top left: IC; top right: Ps; bottom: CVs.

systematics in the NFW spectrum, none of the energy bins shows an excess larger than 1.2σ.

APPENDIX C: SPECTRAL FIT TO EXTRACTED SPECTRAL POINTS

After the spectral extraction per energy bin, the total and component-wise flux data points are analyzed by a spectral fit including the energy redistribution of SPI. This means (astro)physical or empirical models that are parametrized through spectral parameters to predict a differential flux in units of ph cm^{-2} s^{-1} keV^{-1} are convolved with the energy redistribution matrix to account for possible dispersion in the measurement. Thus the differential flux is converted to a rate of photons expected during the measurement time. As an example here, we detail out the spectral model used for the total spectrum; the individual components follow accordingly.

We describe the total spectrum as a linear combination of (a) a cutoff power law to describe the population of unresolved point sources in the Galactic ridge (mainly CVs), (b) a power law to describe the IC scattering component from giga-electron-volt electrons, (c) the positronium emission from the annihilation of cooled cosmic-ray positrons with electrons in the interstellar medium, (d) nuclear lines from massive star and nova ejecta, and (e) the possible contribution from PBHs. From (a) to (e), the models read

$$\text{(a)} \quad C_0 \left(\frac{E}{E_0}\right)^{\alpha_0} \exp\left(-\frac{E}{E_C}\right), \tag{C1}$$

$$\text{(b)} \quad C_1 \left(\frac{E}{E_1}\right)^{\alpha_1}, \tag{C2}$$

$$\text{(c)} \quad f(f_{\mathrm{Ps}}, F_{511}), \tag{C3}$$

$$\text{(d)} \quad \sum_i \left[\frac{F_i}{\sqrt{2\pi}\sigma_i} \exp\left(-\frac{1}{2}\left(\frac{E-\mu_i}{\sigma_i}\right)^2\right)\right] \quad \text{with} \quad F_{60.1} = F_{60.2} = bF_{26}, \tag{C4}$$

$$\text{(e)} \quad g(f_{\mathrm{PBH}}, M_{\mathrm{PBH}}); \text{ see main paper.} \tag{C5}$$

Here, the following parameters are fixed because they either cannot be constrained through the spectrum alone or are mere pivotal parameters: $E_0 = 50$ keV, $E_1 = 1000$ keV, $\alpha_0 = 0$, $\mu_{26} = 1809$ keV, $\mu_{60.1} = 1173$ keV, $\mu_{60.2} = 1332$ keV, $\mu_7 = 478$ keV, $\mu_{22} = 1275$ keV, $\sigma_{26} = 1.7$ keV, $\sigma_{60.1} = 1.5$ keV, $\sigma_{60.2} = 1.5$ keV, $\sigma_7 = 2.4$ keV, and $\sigma_{22} = 8.5$ keV. For all para-meters we use log-uniform priors in a broad range, except for the scaling between the ^{26}Al and the ^{60}Fe lines with $b = 0.18 \pm 0.08$ (see [42]), and the nova lines from ^{7}Be and ^{22}Na for which we use a truncated Gaussian prior bound to zero and widths of 2.0×10^{-4} and 1.3×10^{-4} ph cm^{-2} s^{-1} for F_7 and F_{22}, respectively [43]. The function $f(f_{\rm Ps}, F_{511})$ for the positronium continuum and 511 keV line can be found in Ref. [55] and is only parametrized by the positronium fraction $f_{\rm Ps}$ and the 511 keV line flux F_{511}. Likewise, the function $g(f_{\rm PBH}, M_{\rm PBH})$ is described in detail in the main text and parametrized through the fraction $f_{\rm PBH}$ to account for possible PBH evaporation of a monochromatic PBH mass distribution centered at $M_{\rm PBH}$.

TABLE II. Best fit parameters excluding the PBH component. The units are, from top to bottom, ph cm^{-2} s^{-1} keV^{-1}, keV, 10^{-6} ph cm^{-2} s^{-1} keV^{-1}, 1, 10^{-4} ph cm^{-2} s^{-1}, 1, 10^{-4} ph cm^{-2} s^{-1}, 10^{-4} ph cm^{-2} s^{-1}, 10^{-4} ph cm^{-2} s^{-1}, and 1.

Parameter	Value	Neg. Uncert.	Pos. Uncert.
C_0	3.40	−2.10	1.60
E_C	5.80	−0.60	0.60
C_1	7.00	−0.60	0.60
α_1	−1.24	−0.06	0.06
F_{26}	4.00	−0.50	0.60
b	0.19	−0.07	0.07
F_7	1.70	−1.20	1.20
F_{22}	1.10	−0.80	0.80
F_{511}	13.20	−1.60	1.60
$f_{\rm Ps}$	0.88	−0.09	0.09

The best-fit spectral parameters are summarized in Table II. The method to derive upper bounds on the PBH fraction vs mass is described in detail in the appendix of Ref. [27]. We refer the reader to this publication.

[1] A. M. Green and B. J. Kavanagh, J. Phys. G **48**, 043001 (2021).
[2] C. Winkler *et al.*, Astron. Astrophys. **411**, L1 (2003).
[3] G. Vedrenne *et al.*, Astron. Astrophys. **411**, L63 (2003).
[4] R. Laha, J. B. Muñoz, and T. R. Slatyer, Phys. Rev. D **101**, 123514 (2020).
[5] J. F. Navarro, C. S. Frenk, and S. D. M. White, Astrophys. J. **490**, 493 (1997).
[6] T. Siegert, J. Berteaud, F. Calore, P. D. Serpico, and C. Weinberger, Astron. Astrophys. **660**, A130 (2022).
[7] R. Diehl, T. Siegert, J. Greiner, M. Krause, K. Kretschmer, M. Lang, M. Pleintinger, A. W. Strong, C. Weinberger, and X. Zhang, Astron. Astrophys. **611**, A12 (2018).
[8] T. Siegert, R. Diehl, C. Weinberger, M. M. M. Pleintinger, J. Greiner, and X. Zhang, Astron. Astrophys. **626**, A73 (2019).
[9] T. J. L. Courvoisier, R. Walter, V. Beckmann, A. J. Dean, P. Dubath, R. Hudec, P. Kretschmar, S. Mereghetti, T. Montmerle, N. Mowlavi, S. Paltani, A. Preite Martinez, N. Produit, R. Staubert, A. W. Strong, J. P. Swings, N. J. Westergaard, N. White, C. Winkler, and A. A. Zdziarski, Astron. Astrophys. **411**, L53 (2003).
[10] A. W. Strong, R. Diehl, H. Halloin, V. Schönfelder, L. Bouchet, P. Mandrou, F. Lebrun, and R. Terrier, Astron. Astrophys. **444**, 495 (2005).
[11] L. Bouchet, A. W. Strong, T. A. Porter, I. V. Moskalenko, E. Jourdain, and J.-P. Roques, Astrophys. J. **739**, 29 (2011).
[12] L. Bouchet, P. R. Amestoy, A. Buttari, F. H. Rouet, and M. Chauvin, Astron. Astrophys. **555**, A52 (2013).
[13] R. Krivonos, M. Revnivtsev, E. Churazov, S. Sazonov, S. Grebenev, and R. Sunyaev, Astron. Astrophys. **463**, 957 (2006).
[14] T. Siegert, R. Diehl, G. Khachatryan, M. G. H. Krause, F. Guglielmetti, J. Greiner, A. W. Strong, and X. Zhang, Astron. Astrophys. **586**, A84 (2016).
[15] R. Diehl, H. Halloin, K. Kretschmer, G. G. Lichti, V. Schönfelder, A. W. Strong, A. von Kienlin, W. Wang, P. Jean, J. Knoedlseder, J. P. Roques, G. Weidenspointner, S. Schanne, D. H. Hartmann, C. Winkler, and C. Wunderer, Nature (London) **439**, 45 (2006).
[16] T. A. Porter, G. Johannesson, and I. V. Moskalenko, Astrophys. J. **846**, 67 (2017).
[17] E. V. Karukes, M. Benito, F. Iocco, R. Trotta, and A. Geringer-Sameth, J. Cosmol. Astropart. Phys. 05 (2020) 033.
[18] A. Lutovinov, V. Suleimanov, G. J. M. Luna, S. Sazonov, D. de Martino, L. Ducci, V. Doroshenko, and M. Falanga, New Astron. Rev. **91**, 101547 (2020).
[19] S. Hawking, Mon. Not. R. Astron. Soc. **152**, 75 (1971).
[20] A. Arbey and J. Auffinger, Eur. Phys. J. C 79 (2019).
[21] S. Chen, H.-H. Zhang, and G. Long, Phys. Rev. D **105**, 063008 (2022).
[22] D. Foreman-Mackey, D. W. Hogg, D. Lang, and J. Goodman, Publ. Astron. Soc. Pac. **125**, 306 (2013).
[23] G. Vianello, R. J. Lauer, P. Younk, L. Tibaldo, J. M. Burgess, H. Ayala, P. Harding, M. Hui, N. Omodei, and H. Zhou, arXiv:1507.08343.
[24] A. W. Strong, T. A. Porter, S. W. Digel, G. Jóhannesson, P. Martin, I. V. Moskalenko, E. J. Murphy, and E. Orlando, Astrophys. J. Lett. **722**, L58 (2010).
[25] J. F. Beacom and H. Yüksel, Phys. Rev. Lett. **97**, 071102 (2006).
[26] E. Churazov, S. Sazonov, S. Tsygankov, R. Sunyaev, and D. Varshalovich, Mon. Not. R. Astron. Soc. **411**, 1727 (2011).

[27] T. Siegert, C. Boehm, F. Calore, R. Diehl, M. G. H. Krause, P. D. Serpico, and A. C. Vincent, Mon. Not. R. Astron. Soc. **511**, 914 (2022).
[28] M. Boudaud and M. Cirelli, Phys. Rev. Lett. **122**, 041104 (2019).
[29] W. DeRocco and P. W. Graham, Phys. Rev. Lett. **123**, 251102 (2019).
[30] A. Coogan, L. Morrison, and S. Profumo, Phys. Rev. Lett. **126**, 171101 (2021).
[31] H. Kim, Mon. Not. R. Astron. Soc. **504**, 5475 (2021).
[32] R. Laha, P. Lu, and V. Takhistov, Phys. Lett. B **820**, 136459 (2021).
[33] J. Iguaz, P. D. Serpico, and T. Siegert, Phys. Rev. D **103**, 103025 (2021).
[34] R. Laha, J. B. Muñoz, and T. R. Slatyer, Phys. Rev. D **101**, 123514 (2020).
[35] R. Laha, Phys. Rev. Lett. **123**, 251101 (2019).
[36] F. Calore, M. Cirelli, L. Derome, Y. Genolini, D. Maurin, P. Salati, and P. D. Serpico, SciPost Phys. **12**, 163 (2022).
[37] I. A. Grenier, J. H. Black, and A. W. Strong, Annu. Rev. Astron. Astrophys. **53**, 199 (2015).
[38] A. Merloni *et al.* (eROSITA Collaboration), arXiv:1209.3114.
[39] A. Ray, R. Laha, J. B. Muñoz, and R. Caputo, Phys. Rev. D **104**, 023516 (2021).
[40] J. Auffinger, Eur. Phys. J. C **82**, 384 (2022).
[41] https://galprop.stanford.edu/.
[42] W. Wang, T. Siegert, Z. G. Dai, R. Diehl, J. Greiner, A. Heger, M. Krause, M. Lang, M. M. M. Pleintinger, and X. L. Zhang, Astrophys. J. **889**, 169 (2020).
[43] T. Siegert, S. Ghosh, K. Mathur, E. Spraggon, and A. Yeddanapudi, Astron. Astrophys. **650**, A187 (2021).
[44] L. Bouchet, E. Jourdain, and J.-P. Roques, Astrophys. J. **801**, 142 (2015).
[45] M. Ackermann *et al.*, Astrophys. J. **750**, 3 (2012).
[46] D. Bisschoff, M. S. Potgieter, and O. P. M. Aslam, Astrophys. J. **878**, 59 (2019).
[47] Y. Genolini, M. Boudaud, P. I. Batista, S. Caroff, L. Derome, J. Lavalle, A. Marcowith, D. Maurin, V. Poireau, V. Poulin, S. Rosier, P. Salati, P. D. Serpico, and M. Vecchi, Phys. Rev. D **99**, 123028 (2019).
[48] N. Weinrich, M. Boudaud, L. Derome, Y. Genolini, J. Lavalle, D. Maurin, P. Salati, P. Serpico, and G. Weymann-Despres, Astron. Astrophys. **639**, A74 (2020).
[49] G. L. Case and D. Bhattacharya, Astrophys. J. **504**, 761 (1998).
[50] F. Acero *et al.*, Astrophys. J. Suppl. Ser. **223**, 26 (2016).
[51] S. Recchia, P. Blasi, and G. Morlino, Mon. Not. R. Astron. Soc. **462**, L88 (2016).
[52] S. S. Cerri, D. Gaggero, A. Vittino, C. Evoli, and D. Grasso, J. Cosmol. Astropart. Phys. 10 (2017) 019.
[53] E. Orlando, Mon. Not. R. Astron. Soc. **475**, 2724 (2018).
[54] E. Orlando, Phys. Rev. D **99**, 043007 (2019).
[55] T. Siegert, R. M. Crocker, O. Macias, F. H. Panther, F. Calore, D. Song, and S. Horiuchi, Mon. Not. R. Astron. Soc. **509**, L11 (2021).